Catalysis Science & Technology

ROYAL SOCIETY OF CHEMISTRY

PAPER

View Article Online
View Journal | View Issue

Cite this: *Catal. Sci. Technol.*, 2020, **10**, 1299

Synergy effect between photocatalysis and heterogeneous photo-Fenton catalysis on Ti-doped $LaFeO_3$ perovskite for high efficiency light-assisted water treatment†

Patricia Garcia-Muñoz, *[a] Fernando Fresno,[b] Christophe Lefevre,[c] Didier Robert[a] and Nicolas Keller *[a]

Received 9th November 2019,
Accepted 17th January 2020

DOI: 10.1039/c9cy02269d

rsc.li/catalysis

A strategy combining both heterogenized photo-Fenton and photocatalysis advanced oxidation processes for a single dual catalyst is developed simultaneously benefiting from the higher reaction rate of photo-Fenton and the higher mineralization yield of photocatalysis in water treatment, while overcoming the strong drawbacks still limiting their viability as single processes. We prepared *via* a facile Pechini sol–gel route a highly efficient and stable Ti-substituted $LaFeO_3$ dual catalyst, acting simultaneously as a reusable photo-Fenton solid catalyst and a photocatalyst in water treatment. The partial substitution of La by Ti ions in the crystalline network led to pure heterogeneous surface reactions with an increase in the catalyst robustness by more than two orders of magnitude, indicating the absence of any Fe released and the stability of catalytic performance with test cycles. It further strongly enhanced the reaction rates, due to both increased availability of the photogenerated charge carriers at the surface and the electronic enrichment of surface Fe, and allowed full mineralization of a pollutant to be achieved at circumneutral pH through combined advanced oxidation processes.

Introduction

In addition to increasingly restrictive environmental government regulations, the emergence of biorecalcitrant refractory pollutants in water, the heterogeneity of the targets and the increase in the volume and concentration of polluted water streams have attracted strong interest for the elaboration of new sustainable and cost-effective water treatment technologies.[1–4] In this frame, advanced oxidation processes (AOPs), based on the generation of highly active $HO_x^{\bullet}$ oxidative radicals that react with pollutants and further with reaction intermediates to achieve substrate mineralization, have been developed for removing a large class of refractory substances that cannot be treated through conventional mechanical, biological or physico-chemical water treatments.[5,6]

Among them, (i) the homogeneous Fenton process,[7] or heterogeneous catalytic wet peroxide oxidation (CWPO),[8] that is based on the catalytic decomposition of H_2O_2 in the presence of metallic ions, in most of the cases Fe, and (ii) photocatalysis,[9] that uses the redox surface properties developed by an adequately-irradiated semiconductor, have aroused particular interest because of their high efficiency as well as relatively low investment/running costs, although they operate *via* different mechanisms and under different conditions. However, both processes still suffer from strong limitations that reduce their viability.

While heterogeneous semiconductor photocatalysis is an AOP that takes advantage of its ability to achieve total mineralization of a large variety of refractory organic substances and works within a large pH range, it unfortunately suffers from far lower reaction rates than homogeneous Fenton-like AOPs, and accordingly from far longer process durations.[5,10,11]

By contrast, the viability of the Fenton AOP is strongly reduced by the requirement to operate at acidic pH and by the complexation of Fe with short-chain acids which leads to the generation/precipitation of sludge, with the consequent continuous loss of the active phase and the non-sustainable production of waste.[12] Heterogenization of the Fenton AOP by incorporating Fe in a catalytic body partially overcomes these issues, but at the expense of a strong reduction in the

[a] *Institut de Chimie et Procédés pour l'Energie, l'Environnement et la Santé (ICPEES), CNRS/University of Strasbourg, 25 rue Becquerel, Strasbourg, France. E-mail: garciamunoz@unistra.fr, nkeller@unistra.fr*
[b] *Photoactivated Processes Unit, IMDEA Energy Institute. Avda. Ramón de la Sagra, 3, Parque Tecnológico de Móstoles, 28935 Móstoles, Madrid, Spain*
[c] *Institut de Physique et de Chimie des Matériaux de Strasbourg (IPCMS), CNRS/University de Strasbourg, 23 rue du Loess, Strasbourg, France*

† Electronic supplementary information (ESI) available: SEM and TEM characterization; UPS spectra; crystallographic data of the refined samples (fresh and used); XRD patterns of used samples. See DOI: 10.1039/c9cy02269d

reaction rates in comparison to the homogeneous Fenton counterpart, with a drastic decrease of the process ability to achieve complete pollutant mineralization and continuous Fe release in water by leaching.[7,12] Furthermore, although performing CWPO under light in the so-called photo-assisted CWPO or heterogenized photo-Fenton process is a promising approach for increasing the catalyst reactivity by further boosting the rate-limiting $Fe^{III} \rightarrow Fe^{II}$ conversion in the Fe^{III}/Fe^{II} redox cycle, the above-mentioned drawbacks still limit the viability of the heterogenized catalytic process.[5,7,13]

Therefore, a strategy consisting in combining both heterogenized photo-Fenton and photocatalysis AOPs with a unique catalyst is considered as a promising approach simultaneously benefiting from a higher mineralization yield and a higher reaction rate, with as key-features that this unique dual catalyst works under similar reaction conditions as a heterogeneous photocatalyst and a Fe-based photo-Fenton catalyst without any loss of the Fe active phase with time-on-run. Meanwhile, physical mixtures of catalysts have been tested,[14–17] and the design of a single catalyst combining both AOPs has been scarcely reported, notably using $ZnFe_2O_4$ spinel ferrite, natural Fe oxide or Ba-doped $BiFeO_3$ perovskite.[18–20]

Here, we report on the use of Ti-substituted lanthanum ferrite ($LaFeO_3$) perovskite catalysts in water treatment acting simultaneously as a heterogenized photo-Fenton catalyst and a photocatalyst under similar circumneutral pH reaction conditions for achieving complete mineralization of a substrate under UV-A light with strongly enhanced reaction rates, while improving the catalyst stability by totally inhibiting the Fe release in water. This new dual catalyst is based on a $LaFeO_3$ semiconductor that is one of the most common ABO_3 perovskite oxides studied in many research fields such as solid oxide fuel cells, optoelectronics, magnetism, gas sensors or heterogeneous thermal catalysis, because it takes advantage of its $A_{1-x}A'_xB_{1-y}B'_yO_{3\pm\delta}$ composition versatility that allows notably its textural, structural or electronic properties to be modified, and as a result, its redox and catalytic ability to be tuned through A- and/or B-site cationic partial substitution.[21] Its composition is consequently in agreement with the sustainability need currently in force that requires the use of cheap, abundant, and environmentally non-toxic elements in chemical processes.[22] While cation-doped $LaFeO_3$ ferrites have been mainly used till now as photo Fenton catalysts, their use also as photocatalysts remained scarce. Here, the removal of 4-chorophenol (4-CP) has been selected as the test reaction in water under UV-A light, as 4-CP is a model molecule used in AOP studies as a representative of industrial wastewater refractory pollutants,[23–25] while some mineralization tests were also performed using the myclobutanil $C_{15}H_{17}ClN_4$ triazole as an antifungal substrate in order to broaden the scope of the work.[26,27]

Experimental

Synthesis of Ti-substituted $LaFeO_3$

$La_{1-x}Ti_xFeO_3$ catalysts were prepared by modifying the sol–gel Pechini synthesis. $La(NO_3)_3$ lanthanum nitrate hexahydrate (108.3 g L^{-1}, 99.9%, Sigma Aldrich) and $Fe(NO_3)_3$ iron nitrate nonahydrate (133 g L^{-1}, 99.95%, Sigma Aldrich) were dissolved in stoichiometric amounts in distilled water (30 mL), and the metallic ions underwent complexation by subsequent addition of citric acid ($C_6H_8O_7xH_2O$, 70 g L^{-1}, 99.5%, Sigma Aldrich) in a stoichiometric molar ratio with respect to the metallic ions.

A titanium source was introduced under stirring into the aqueous sol and the resulting suspensions were maintained at 80 °C for 48 h (2 °C min^{-1} heating rate) in order to induce the complete gel formation. The calcination of the dried gel was performed using a heating cycle as reported by Gosavi *et al.*[28] with a heating rate of 5 °C min^{-1}, holding the temperature at 600 °C for 2 h, before subsequently maintaining a temperature plateau at 800 °C for 2 h.

In the synthesis of the P25-LFO catalyst, commercial TiO_2 Aeroxide© P25 powder (hydrophilic fumed titanium dioxide, ≥99.50%, Evonik, Germany) that consists of a mixture of anatase and rutile crystalline phases in a 80/20 molar ratio was used as a titanium source.

In the synthesis of the SG-LFO catalyst, dried amorphous titania was used as a titanium source. It was obtained according to a sol–gel synthesis method under basic conditions using titanium tetraisopropoxide (TTIP, 97%, Sigma-Aldrich) as a precursor. In a typical synthesis, 17.8 g of TTIP was first added to a 40 mL ethanolic solution, before a similar volume of water was added dropwise to the solution. After rectification of the pH to 9 by adding ammonia (Carlo Erba, 30% aqueous solution), the solution was left under agitation at room temperature until a dry paste was obtained. The resulting powder was further dried at 110 °C for 12 h to obtain the dried amorphous titania used as a titanium source in the modified sol–gel Pechini synthesis.

Regardless of the titanium source, the titanium added during the Pechini synthesis corresponded to a nominal amount of 10 wt% in terms of TiO_2 with respect to the theoretical amount of $LaFeO_3$ perovskite obtained. Non-modified lanthanum ferrite powders have been synthesized as reference materials *via* the same protocol without any addition of titanium source, with a similar calcination procedure.

The stoichiometric reaction forming the $LaFeO_3$ perovskite is as follows (eqn (1)):[29]

$$La(NO_3)_3x6H_2O + Fe(NO_3)_3x9H_2O + C_6H_8O_7xH_2O \rightarrow LaFeO_3 + 6CO_2 + 3N_2 + nH_2O \quad (1)$$

The reference titanium-free material was labelled as LFO, while the Ti-modified materials were labelled as P25-LFO and SG-LFO when using Aeroxide© TiO_2 P25 and dried amorphous titania as titanium sources, respectively.

Characterisation techniques

The reference X-ray diffraction (XRD) patterns were recorded at room temperature in a θ/θ mode on a Bruker D8 Advance diffractometer equipped with a monochromatic copper

radiation source (Kα = 1.54056 Å) with a scan step of 0.02°. Some patterns have been investigated by Rietveld refinement with the Fullprof software for which the modified Thompson–Cox–Hasting function was chosen to generate the line shape of the diffraction peaks. Instrumental broadening was previously determined by measuring the scattering from corundum (NIST standard SRM 1976b).[30,31]

Scanning electron microscopy (SEM) was performed in secondary electron mode on a JEOL JSM-6700 F FEG microscope.

Transmission electron microscopy (TEM) was performed using a JEOL 2100F with a 0.2 nm point resolution. A copper grid covered by a holey carbon membrane was used for observation. The interplanar spacings were calculated using ImageJ software.

UV-vis diffuse reflectance spectra were acquired using a UV/vis/NIR Perkin Elmer Lambda 1050 spectrometer, recording the reflectance between 250 and 800 nm. Band gaps were estimated from Tauc plots represented by $(\alpha h\nu)^2$ *vs.* photon energy, where α = −ln(reflectance), in accordance with the direct semiconductor character of $LaFeO_3$.[32]

The fluorescence spectra of the powdered samples were recorded with a fluorescence spectrometer Perkin Elmer LS55, using an excitation wavelength of 450 nm and a cut-off filter at 515 nm. Fluorescence lifetime measurements by time-correlated single photon counting (TCSPC) were carried out with Mini-τ equipment from Edinburgh Instruments using a laser diode (model EPL375) as an excitation source with a wavelength of 445.2 nm and a pulse width of 90.7 ps, at a repetition rate of 1 MHz, with a band pass filter at 600 ± 25 nm. The decay profiles were fitted to a bi-exponential decay curve, with lifetimes obtained as the average of both components, calculated as $\langle\tau\rangle = [\sum(A_i\tau_i^2)]/\sum(A_i\tau_i)$, where A_i is the amplitude and τ_i the lifetime of each component.

X-ray photoelectron spectroscopy (XPS) analysis was performed on a ThermoVGMultilabESCA3000 spectrometer (Al K_α anode at $h\lambda$ = 1486.6 eV). The energy shift due to electrostatic charging was subtracted using the contamination sp^2 carbon C 1s band at 284.6 eV. Contributions with a Doniach–Sunjic shape[33] and an S-shaped Shirley type background[34] were used.

Degradation test protocol

The 4-CP and myclobutanil degradation tests were performed in a batch beaker-type glass reactor at atmospheric pressure, at a constant temperature of 20 °C ± 2 °C (using a cooling bath) with H_2O_2 as the main oxidant. In a typical reaction procedure, 50 mg of catalyst was dispersed under stirring in a 100 mL aqueous solution of 4-chlorophenol at a concentration of 25 mg L^{-1}, corresponding to an initial organic carbon concentration of 14.8 ppm and to a catalyst load of 0.5 g L^{-1}. For the reactions with myclobutanil, a starting concentration of 20 mg L^{-1} of the pollutant was selected. Prior to irradiation, the catalyst suspension was stirred for 1 h in the dark to ensure the establishment of the adsorption/desorption equilibrium. After adding H_2O_2 at the stoichiometric concentration corresponding to the complete mineralization of the initial pollutant (125 mg L^{-1}), or substoichiometric in some cases (31.25 and 62.50 mg L^{-1}), the tests were performed under UV-A (60 W m^{-2}; λ = 365 nm, Philips 24 W/10/4P lamps). At each time interval, 8 mL of solution was sampled and then filtered through a 0.20 μm porosity filter to remove the photocatalyst powder if any, before the concentration of 4-chlorophenol or myclobutanil was determined by UV-visible spectrophotometry by following the disappearance of the main absorption peak at λ = 224 nm.[35] Total organic carbon measurements were carried out using a Shimadzu TOC-L analyzer to determine the organic carbon load. The H_2O_2 concentration was measured by colorimetric titration using the $TiOSO_4$ method[36] and the Fe leached during the time-course of the reaction was quantified by the *ortho*-phenanthroline method.[37]

Tests with myclobutanil as the substrate were performed following a similar test protocol, at a myclobutanil concentration of 20 mg L^{-1}. The myclobutanil concentration was determined by UV-visible spectrophotometry by monitoring the disappearance of the main absorption peak at λ = 220 nm.

Results and discussion

Catalyst characterization

Fig. 1 shows the XRD patterns of the pristine and Ti-modified $LaFeO_3$ materials with their corresponding Rietveld refinement profiles. Tables 1 and S1† show the refined cationic distribution in the $LaFeO_3$ structure and the crystallographic data, respectively. The XRD patterns of the pristine catalyst exhibited the most intense diffraction peaks at 22.6°, 32.2°, 39.7°, 46.1°, 57.4° and 67.3° in 2θ, corresponding to the diffraction of the (100), (110), (111), (200), (210) and (220) planes of the $LaFeO_3$ phase, respectively. α-Fe_2O_3 in a small amount (11%) with a mean crystallite size of 35 nm was observed as the extra phase. In the Ti-doped samples, independent of the Ti source, all the patterns can be indexed to the *Pbnm* orthorhombic unit cell of $LaFeO_3$, with no change in terms of α-Fe_2O_3 additional phase. Neither La_2O_3 nor TiO_2 is observed as the extra phase. Elemental chemical analysis reveals a 3.2 at% Ti content in the Ti-modified $LaFeO_3$ catalyst prepared using the crystalline TiO_2 nanopowder as the precursor, which further increased up to 4.0 at% using the dried amorphous precursor, while the Ti/Fe molar ratio remains unchanged (Table 2).

The separate refinement of both Ti/Fe and Ti/La site occupations evidences that titanium atoms preferentially occupy exclusively the La A-site and substitute only the La atoms, so that the catalysts can be labelled as $La_{1-x}Ti_xFeO_3$. A partial Ti → La substitution rate of 5 at% was achieved within the perovskite network in the A-site using the crystalline TiO_2 nanopowder as the titanium precursor, while it increases up to 11 at% using the dried amorphous precursor (Table 1). The exclusive La A-site occupation is rather unexpected when considering the involved cationic sizes – $(r_{Fe+III})_{CN=6}$ = 0.64,

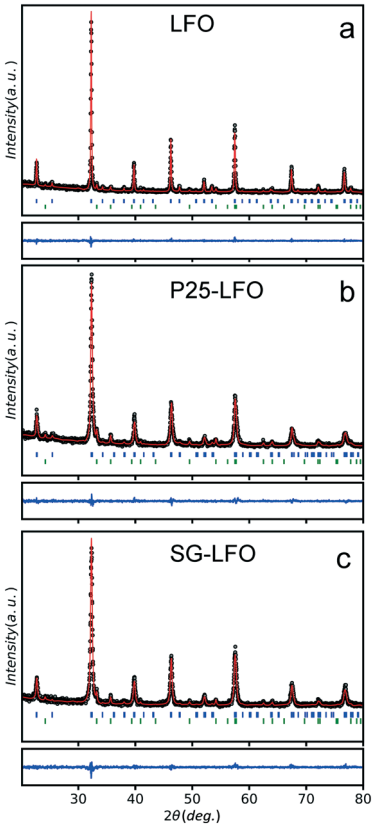

Fig. 1 Observed (black), calculated (red full line), and difference (blue full line) X-ray powder diffraction patterns of (a) LFO, (b) P25-LFO and (c) SG-LFO catalysts recorded on a D8 diffractometer (λ = 1.54056 Å). The positions of the Bragg reflections are represented by vertical bars, in blue for the reflections indexed in the *Pbnm* orthorhombic unit cell of $LaFeO_3$ and in green for those of the α-Fe_2O_3 extra phase.

$(r_{La+III})_{CN12}$ = 1.46 and $(r_{Ti+III})_{CN=6}$ = 0.76.[38] Both A- and B-site substitutions have been reported for the $LaFeO_3$ structure depending on the doping element, although high valence metal ions usually occupy the Fe^{3+} sites.[39,40] However, there is no empirical rule on the location of the substituting element depending on the electronic or steric criterion, and many extrinsic parameters are known to affect the cationic distribution in oxides, *e.g.* the cooling rate or the synthesis temperature.[41,42] Here, we suggested that the partial substitution resulted from temperature-driven solid–solid diffusion that is proposed to occur between the amorphous $LaFeO_3$ network – before it crystallizes – and the TiO_2 crystallites, allowing the Ti atoms to distribute in the $LaFeO_3$ network. Consequently, replacing the well-crystallized TiO_2 nanoparticles with a 22 nm average size by an amorphous network increased further the substitution rate by favouring the atomic titanium diffusion in the amorphous $LaFeO_3$ perovskite network. In addition, this partial substitution hindered the growth of large crystallites during the temperature-driven crystallization at 800 °C when compared to the undoped counterpart (20–21 nm *vs.* 46 nm), as previously observed for Li- or Cu-doped $LaFeO_3$ materials.[43,44] An increase in the specific surface area from 8 to 28 $m^2\ g^{-1}$ was simultaneously observed for the P25-LFO catalyst as a result of the decrease in mean crystallite size, as shown in Table 2. However, the SG-LFO catalyst displayed a low specific surface area of 5 $m^2\ g^{-1}$, although it displayed a smaller mean crystallite size of 20 nm. This was attributed to the existence of more grain boundaries within the SG-LFO materials compared to the P25-LFO counterpart.

While the SEM images shown in Fig. S1† evidenced the overall powder morphology of the catalysts, the TEM images shown in Fig. S2† and in Fig. 2 confirmed the structural features of both the pristine LFO and the SG-LFO catalysts, respectively. Whether the catalyst was doped or not with titanium, interplanar spacings of 0.39 nm, 0.28 nm and 0.23 nm consistent with the (110), (100) and (111) planes characteristic of the $LaFeO_3$ structural crystallographic features were observed.

The ability of the $La_{1-x}Ti_xFeO_3$ materials to be used as photocatalysts under UV-A light is confirmed by the UV-vis absorbance spectra, that reveal a broad absorption band in the UV-vis range, and a band-gap estimated graphically from the Tauc plots at 2.1 eV whether the catalyst contained substitutional titanium or not (Fig. 3).

In order to shed light on the effects of Ti → La substitution, further characterization of the doped and undoped samples was performed. The fluorescence spectra shown in the inset of Fig. 4 showed the emission profile of $LaFeO_3$ with a main contribution centered at *ca.* 485 nm, similar to what has been reported for lanthanum ferrite,[45] which can be associated with the direct radiative de-excitation of electrons from high-energy levels within the conduction band to the valence band.[45,46]

Table 1 Refined cationic distribution in the $La_{1-x}Ti_xFeO_3$ perovskite catalysts and weight percentage of extra phases obtained after Rietveld refinement

	La site distribution[a]		Fe site distribution[a]	α-Fe_2O_3, %	TiO_2, %
Catalyst	La	Ti	Fe		
LFO	1	0	1	11	0
P25-LFO	0.95	0.05	1	15	0
SG-LFO	0.89	0.11	1	18	0
SG-LFO #1[b]	0.88	0.12	1	12	0
SG-LFO #3[b]	0.88	0.12	1	11	0
SG-LFO #5[b]	0.88	0.12	1	12	0

[a] The determination of the cationic distribution within the structures was performed considering that titanium can move towards both cationic sites. [b] SG-LFO #1, #3 and #5 correspond to the SG-LFO catalyst after tests #1, #3 and #5, respectively.

Table 2 Main physico-chemical properties of the pristine and the Ti-substituted $LaFeO_3$ perovskite catalysts

Catalyst	TiO_2 precursor	Fe[a] (at%)	Ti[a] (at%)	Ti/Fe molar ratio	S_{BET}[b] ($m^2\ g^{-1}$)	D[c] (nm)
LFO	—	23.0	—	—	8	46(1)
P25-LFO	Crystalline anatase/rutile	16.0	3.2	0.23	28	21(1)
SG-LFO	Amorphous hydroxide	22.7	4.0	0.21	5	20(1)

[a] The iron and titanium contents in the catalysts were determined by inductively coupled plasma optical emission spectroscopy (ICP-OES) carried out on an Optima 7000 DV spectrometer (Perkin Elmer), after microwave-assisted acidic dissolution in *aqua regia* at 185 °C under autogenic pressure. [b] The Brunauer–Emmett–Teller (BET) specific surface area was calculated from the N_2 adsorption isotherm recorded on a Micrometrics Tristar 3000 using N_2 as the adsorbent at −196 °C with prior outgassing at 250 °C overnight to desorb the impurities or moisture. [c] The mean crystallite size defined as the average size of the coherent diffracting domains was derived from the whole XRD patterns after refinement and determined using the Scherrer equation with the usual assumption of spherical crystallites taking into account the intrinsic broadening of the peaks due to the instrumentation.

Lower intensity emission at energies lower than the band gap reflects excitonic photoluminescence which is usually associated with sub-band-gap transitions from electronic states related to surface defects or oxygen vacancies.[46]

Upon titanium doping, the positions of the emission bands remain unchanged, while some changes in the intensity are visible, depending on the involved feature. Thus, the high-energy emission is somewhat quenched in the presence of the dopant, which has been associated to a first approximation with a decreased direct recombination rate due to improved charge separation within the semiconductor structure, and consequently with enhanced photocatalytic activity.[47,48] In contrast, the reverse effect of doping is found on the intensity the sub-band-gap features, which can be related to a higher content of surface vacancies/defects in the doped systems.[46] The fluorescence lifetime should nevertheless give more accurate information than the steady-state spectra about recombination kinetics.[49] The fluorescence decay curves for the different samples between 550 and 600 nm, corresponding to the band gap energy shown in Fig. 4, give fluorescence lifetimes of the same order as previously reported values for $LaFeO_3$ and related structures.[47,50] As observed in the curves and the average lifetime values from curve fittings, the P25-LFO sample gives rise to a slightly higher lifetime than the pristine LFO ferrite, while the SG-LFO sample is characterized by a considerably longer fluorescence lifetime, indicative of slower radiative recombination kinetics, which can be ascribed to enhanced charge separation and therefore higher availability of photogenerated electrons and holes for the subsequent surface redox reactions.[47,49,51]

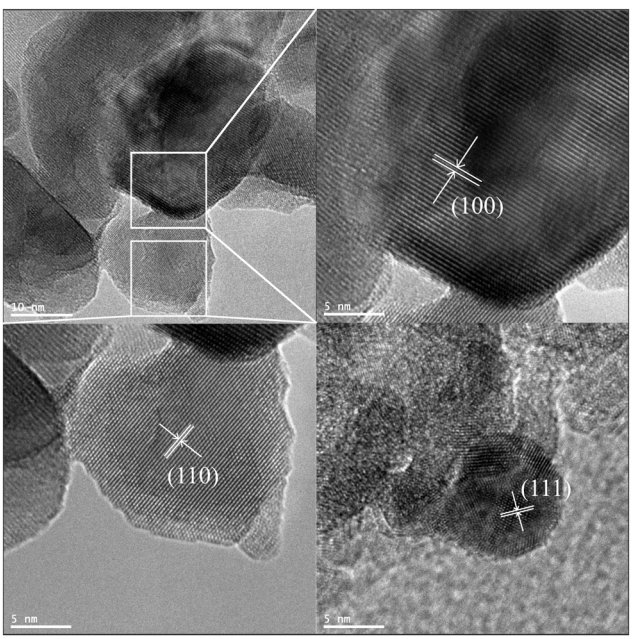

Fig. 2 TEM images of the SG-LFO catalyst. The interplanar distances of 0.39 nm, 0.28 nm and 0.23 nm corresponded to the (110), (100) and (111) planes of the LFO structure, respectively.

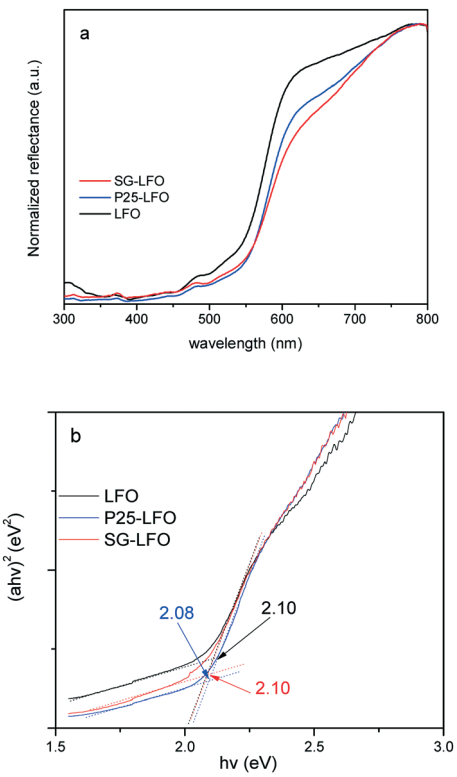

Fig. 3 UV-vis diffuse reflectance spectra (a) and Tauc plots (b) of the LFO, P25-LFO and SG-LFO catalysts. The numerical values in (b) indicate the band gap energies estimated from the Tauc plots.

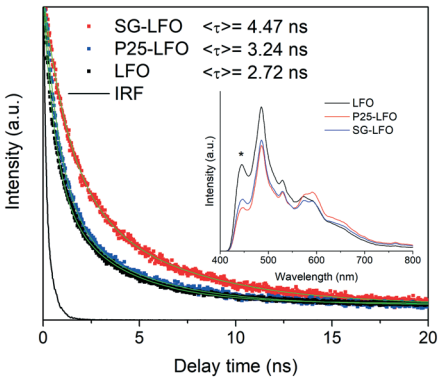

Fig. 4 Fluorescence decay curves of the pristine and Ti-doped $LaFeO_3$ samples between 575 and 625 nm. The green lines correspond to the decay curves fitted to each dataset. $<\tau>$ represents the average fluorescence lifetimes. The instrument response function (IRF) has been included for comparison. Inset: Fluorescence spectra of the same samples; the signal marked with (*) corresponds to the lamp emission as confirmed by recording the emission spectra with different excitation wavelengths.

Fig. 5 shows the influence of the partial substitution of La ions by Ti ions in the LFO structure on the surface state of the SG-LFO catalyst. The XPS analysis revealed the presence of both cations as La^{3+} and Fe^{3+} ions at the surface of the pristine LFO and the SG-LFO catalyst. Indeed, the La 3d core level spectra recorded for the pristine LFO material exhibited a La $3d_{5/2-3/2}$ orbital doublet contribution at 833.4 eV and 850.1 eV, with a 16.7 eV spin orbit splitting[52–54] and a 3.8 eV multiplet splitting,[55] that is characteristic of La^{3+} species. The binding energies of the Fe $2p_{3/2-1/2}$ orbital doublet contribution at 710.3 eV and 723.7 eV, with a spin orbit coupling of 13.4 eV[54,55] and with the broad and low intensity shake-up satellite peak at about 718 eV characteristic of Fe^{3+},[56,57] confirmed the presence of Fe^{3+} ions at the surface of the pristine LFO.

After the Ti → La partial substitution in the LFO perovskite, the XPS Ti 2p profile of the SG-LFO catalyst displayed a single contribution, with the doublet related to Ti $2p_{3/2-1/2}$ spin–orbit components at 457.3 eV and 463.0 eV. This revealed the stabilization of Ti cations at the surface as lower oxidation state Ti^{3+} in the substitution of La^{3+} in the perovskite structure,[55] or as Ti^{4+}–O–M with a strong lower binding energy than Ti^{4+} in an usual TiO_2 network environment (Fig. 5).[58] Further, this led also to a slight downward (−0.7 eV) shift for the binding energies of the Fe 2p orbital doublet contribution at 709.7 eV and 723.2 eV, and simultaneously in a slight upward (+0.8 eV) shift for the La 3d orbital doublet

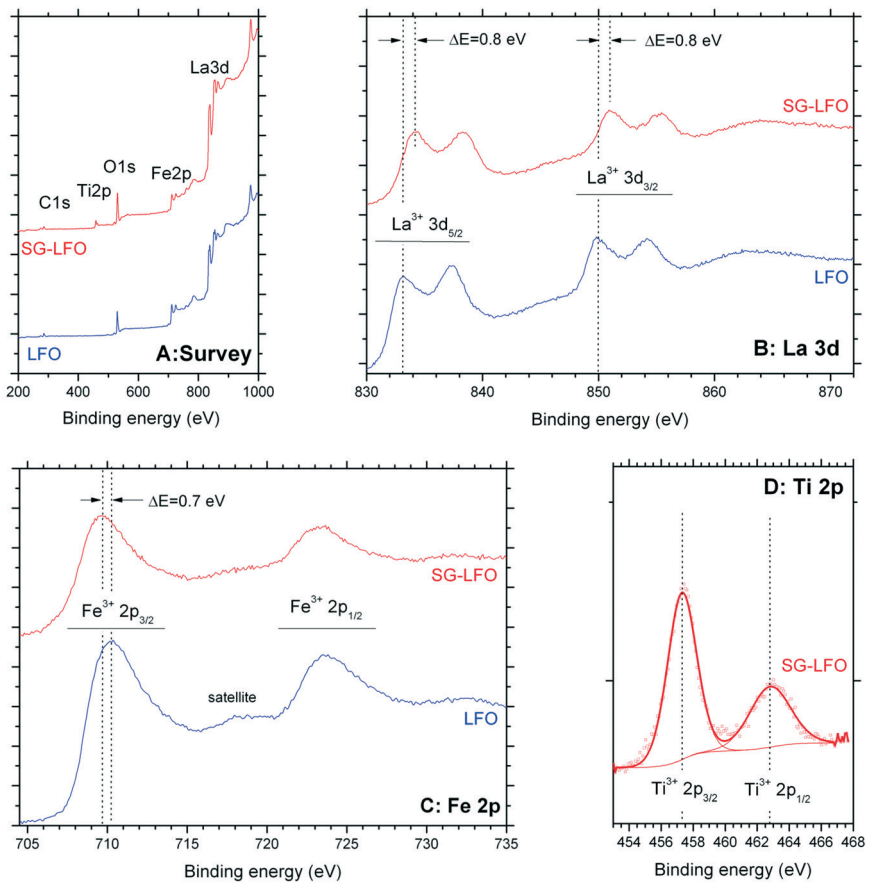

Fig. 5 XPS profiles recorded for both the Ti-free LFO and the SG-LFO catalysts: (A) wide scan survey spectrum, (B) La 3d, (C) Fe 2p and (D) Ti 2p orbitals.

contribution at 834.2 eV and 850.9 eV, both cations remain present at the surface in the formal +3 oxidation state.

According to the electrostatic model, in the Ti–O–La configuration, the upward shift observed for La^{3+} compared to the La–O–La reference configuration results from the higher electronegativity of Ti *vs.* La, that causes a O → Ti shift of the electronic density, and consequently a La → O shift of the La–O bond electronic density, that corresponds to a higher binding energy of La core electrons. So, in contrast, the downward shift of the Fe^{3+} binding energy was assigned to the electronic enrichment of Fe cations, resulting in the lower binding energy of Fe core electrons.

In addition, by combining the UV-vis diffuse reflectance and UPS data, it can be assumed that the partial cationic substitution did not significantly alter neither the potential of the conduction band edge, nor the valence band maximum, determined by UPS (He I, $h\lambda$ = 21.2 eV) at *ca.* 2.2 ± 0.1 eV *vs.* Fermi level whether the surface is modified or not by titanium (Fig. S3†).

Catalytic activity

Combined photo-assisted CWPO and photocatalysis. The evolution with time under irradiation of the main features followed during the reaction is shown in Fig. 6. First, although the titanium-free $LaFeO_3$ catalyst showed the ability to decompose fully H_2O_2 and to remove 4-CP within 150 min of test, it only allowed a mineralization of 75% to be achieved. Further, the catalyst suffered from strong iron leaching, an iron release in the 0.5 mg L^{-1} solution. The low stability of the catalyst resulted in a high contribution of the homogeneous photo Fenton reaction to the H_2O_2 decomposition, and consequently to both 4-CP and TOC removal rates, so that the apparent kinetic rate constants obtained could not be ascribed to a pure heterogeneous process and were therefore over-estimated. This homogeneous contribution was responsible for a low H_2O_2 efficiency value of 0.75, and the resulting incomplete mineralization of the substrate, as typically observed in CWPO-like reactions. Indeed, iron in solution is known to react with the latest degradation intermediates, that are short-chain acids like oxalic, acetic or formic acids, to form highly stable iron complexes that photodegrade very slowly and consequently stop the reaction (eqn (2)).[59–61]

$$\left[Fe^{3+}(RCOO^{-})\right]^{2+} \xrightarrow{h\nu} Fe^{2+} + CO_2 + R \quad (2)$$

In the case of the $La_{1-x}Ti_xFeO_3$ catalysts, the incorporation of titanium atoms into the perovskite network with the Ti → La partial substitution increases considerably the robustness of the catalyst by more than two orders of magnitude. This was evidenced by a strong decrease in the iron release to 0.05 mg L^{-1} for a 5% substitution rate (P25-LFO), and by a further reduction down to the non-detectable level (below 0.001 mg L^{-1}, *i.e.* lower than 0.0009% relative to the catalyst Fe content) for the SG-LFO catalyst with a 11% substitution rate. This increase in stability is accompanied by strong enhancement of the catalytic activity, more pronounced as the substitution rate increases. Thus the duration necessary for achieving the full removal of 4-CP is

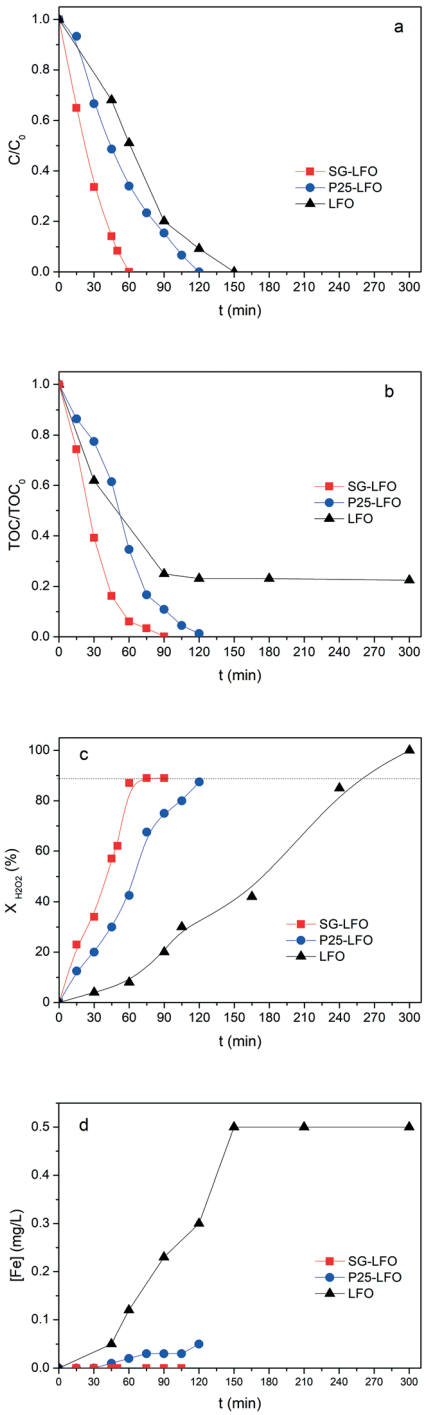

Fig. 6 Evolution with time under irradiation of a) the relative 4-CP concentration, b) the relative TOC concentration, c) the H_2O_2 decomposition yield and d) the concentration of leached Fe in the solution, during the combined photo-Fenton and photocatalytic degradation of 4-CP over the pristine and the Ti-substituted $LaFeO_3$ catalysts. Conditions: $[4\text{-CP}]_0$ = 25 mg L^{-1}; $[H_2O_2]_0$ = 125 mg L^{-1}; T = 25 °C; [cat] = 0.5 g L^{-1}; UV-A irradiance of 60 W m^{-2}.

reduced to 120 min and 60 min for the P25-LFO and SG-LFO catalysts, respectively, while both catalysts achieve complete mineralization within 125 min and 90 min of reaction, respectively. This very good behaviour is reflected in a strong increase in the apparent kinetic constants for 4-CP degradation, TOC conversion and H_2O_2 decomposition (Table 3). The absence of any detectable released iron demonstrates that the strong increase in the catalytic activity can be ascribed to pure heterogeneous surface reactions, without any homogeneous contribution.

Further, both $La_{1-x}Ti_xFeO_3$ catalysts exhibit a H_2O_2 efficiency ξ greater than 1, which reflects the fact that they allow full TOC conversion to be achieved at incomplete H_2O_2 conversion. This evidences that the $La_{1-x}Ti_xFeO_3$ catalysts can act as a dual catalyst, by working simultaneously as a heterogenized photo-Fenton catalyst and a photocatalyst. This dual behaviour was confirmed by the evolution of the TOC conversion with the H_2O_2 conversion shown in Fig. 7a. While the curve obtained for the titanium-free $LaFeO_3$ catalyst is distorted by the strong homogeneous Fenton contribution, the clear distribution of the whole data set for both catalysts above the unity diagonal confirms that the heterogeneous photo-Fenton process cannot be considered as the only AOP operating for converting the TOC. Additional experiments performed using non-stoichiometric H_2O_2 doses underlined further that the TOC conversion is obtained simultaneously through both photo-Fenton and photocatalysis AOPs (Fig. 7b). Indeed, complete TOC conversion was achieved following zero-order kinetics with a similar apparent kinetic rate constant independent of the H_2O_2 dose at 25% or 50%, while the decomposition of H_2O_2 was already completed. This confirms that pure photocatalysis took place allowing full TOC conversion to be obtained.

Although the incorporation of Ti atoms into the LFO network strongly increases the activity in pure photocatalysis, more pronounced as the Ti → La partial substitution increases, the activity remains far lower than that obtained using H_2O_2 (Fig. 8 and Table 4). This corroborates the fact that, in the combined AOPs, the dual $La_{1-x}Ti_xFeO_3$ catalyst acts predominantly as a heterogeneous photo-Fenton catalyst at the beginning of the process, so that high reaction rates can be obtained, while it subsequently operates as a photocatalyst for mineralizing the short chain acids, and consequently allows full TOC conversion to be achieved by hindering the detrimental formation of stable Fe complexes.

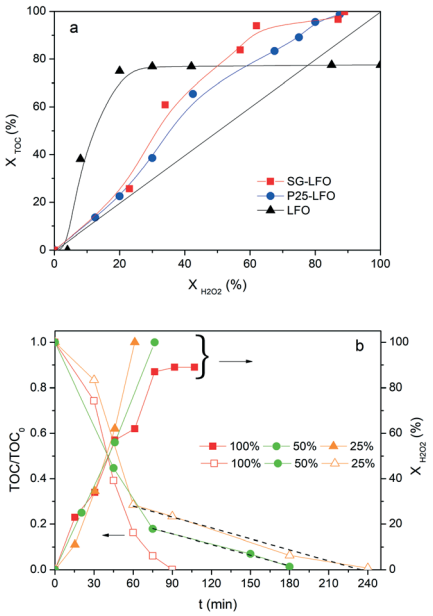

Fig. 7 a) TOC conversion *vs.* H_2O_2 conversion for the combined photo-Fenton and photocatalytic degradation of 4-CP over the pristine and the Ti-substituted $LaFeO_3$ catalysts. Conditions: $[4\text{-CP}]_0$ = 25 mg L^{-1}; $[H_2O_2]_0$ = 125 mg L^{-1}; T = 25 °C; [cat] = 0.5 g L^{-1}; UV-A irradiance of 60 W m^{-2}. b) Influence of the H_2O_2 dose on the relative TOC concentration time-evolution and the H_2O_2 conversion obtained for the SG-LFTO catalyst. Conditions: $[4\text{-CP}]_0$ = 25 mg L^{-1}; $[H_2O_2]_0$ = 31.25–125.00 mg L^{-1}, corresponding to the 25–100% range; T = 25 °C; [cat] = 0.5 g L^{-1}; UV-A irradiance of 60 W m^{-2}. Taking into account that the experiments were carried out using the stoichiometric amount of H_2O_2 to mineralize TOC, the linear curve with a unity slope reflects the implementation of an heterogenized photo-Fenton process with no occurrence of scavenging reactions.

It is worth noting that, although the P25-LFO catalyst might take advantage the enhanced surface area of 28 m^2 g^{-1} for exposing more surface iron active in the decomposition of H_2O_2, the specific surface area of the catalysts cannot be the key factor driving the catalytic activity, since the most active SG-LFO catalyst displays a low surface area of 5 m^2 g^{-1}. We propose therefore that a combination of surface and

Table 3 Kinetic rate constants of H_2O_2 decomposition, 4-CP oxidation, and mineralization through combined photo-Fenton and photocatalysis AOPs. Fe leached, H_2O_2 depletion percentage, TOC conversion and H_2O_2 efficiency parameters. Conditions: $[4\text{-CP}]_0$ = 25 mg L^{-1}; $[H_2O_2]_0$ = 125 mg L^{-1}; T = 25 °C; [cat] = 0.5 g L^{-1}; UV-A irradiance of 60 W m^{-2}

Catalyst	k (H_2O_2),[a] min^{-1}	k (4-CP),[a] min^{-1}	r_0 (TOC),[b] mg L^{-1} min^{-1}	[Fe] leached, mg L^{-1}	X (H_2O_2), %	X (TOC), %	ξ (H_2O_2)[c]
LFO	0.010	0.020	0.12	0.5	100	75	0.75
P25-LFO	0.017	0.017	0.18	0.05	90	100	1.11
SG-LFO	0.043	0.033	0.28	<0.001[d]	89	100	1.12
1–5# reuse of SG-LFO	—	33.3 ± 0.3 10^{-3}	0.28 ± 0.01	<0.001[d]		100	

[a] The H_2O_2 and 4-CP concentration evolution curves were fitted by a pseudo first-order kinetic model as usually applied. [b] The TOC concentration evolution curve was fitted with a zero-order kinetic model as usually applied. [c] A theoretical ξ = 1 efficiency of H_2O_2 used in Fenton-like processes reflects the fact that H_2O_2 and the formed radicals do not suffer from any detrimental scavenger reactions. [d] The detection limit of Fe leached in the solution was measured at 0.001 ppm.

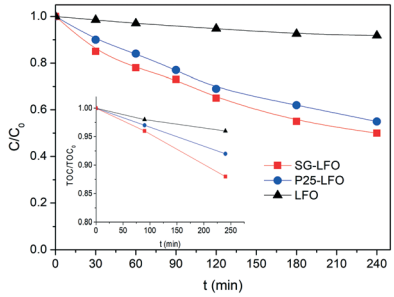

Fig. 8 Time-evolution of both the C/C_0 and TOC/TOC_0 relative concentrations during the pure photocatalytic degradation of 4-CP over the pristine and the Ti-substituted $LaFeO_3$ catalysts. Conditions: $[4\text{-CP}]_0$ = 25 mg L^{-1}; T = 25 °C; [cat] = 0.5 g L^{-1}; UV-A irradiance of 60 Wm^{-2}.

electronic modifications modulates the activity of the $La_{1-x}Ti_xFeO_3$ catalysts and leads the SG-LFO catalyst to exhibit the best catalytic results. On the one hand, electron-rich surface iron enables faster H_2O_2 decomposition by the Fe surface sites, and therefore the production of higher concentrations of active radicals during the Fe^{III}/Fe^{II} redox cycle (eqn (3)–(5)). We may assume that the photoassisted Fe^{3+} to Fe^{2+} reduction in eqn. (4) might be accompanied by Ti^{3+} to Ti^{4+} oxidation as a plausible way of compensating the charge. The Ti^{4+} species might further be reduced back to Ti^{3+} by a photogenerated electron.

$$La_{1-x}Ti_x\,Fe^{III}O_3 + H_2O \xrightarrow{h\nu} La_{1-x}Ti_x\,Fe^{II}O_3 + HOO^{\bullet} + H^+ \quad (3)$$

$$La_{1-x}Ti_x\,Fe^{III}O_3 \xrightarrow{h\nu} La_{1-x}Ti_x\,Fe^{II}O_3 \quad (4)$$

$$La_{1-x}Ti_x\,Fe^{II}O_3 + H_2O_2 \xrightarrow{h\nu} La_{1-x}Ti_x\,Fe^{III}O_3 + HO^{\bullet} + OH^- \quad (5)$$

Further, the degradation of the short-chain acids and consequently the mineralization of the carboxylic acids might be favored by the electronic enrichment of the surface Fe according to eqn (6), with the simultaneous $Fe^{III} \rightarrow Fe^{II}$ surface reduction, known as the rate limiting step in the Fe redox cycle.

$$\left[Fe^{III}(RCOO^-)\right]^{2+} \xrightarrow{h\nu} Fe^{II} + CO_2 + R \quad (6)$$

On the other hand, the enhanced availability of the photogenerated charge carriers also enables more efficient photocatalytic decomposition of H_2O_2, with the production of $HO_x^{\bullet}$ radicals (eqn (7)–(9)), as well as more efficient production of $OH^{\bullet}$ radicals from adsorbed water (eqn (10)).

$$La_{1-x}Ti_x\,FeO_3 \xrightarrow{h\nu} e^- + h^+ \quad (7)$$

$$e^- + H_2O_2 \rightarrow HO^{\bullet} + OH^- \quad (8)$$

$$h^+ + H_2O_2 \rightarrow HOO^{\bullet} + H^+ \quad (9)$$

$$h^+ + H_2O \rightarrow HO^{\bullet} + H^+ \quad (10)$$

The stabilization of Fe^{3+} cations within the orthorhombic $La_{1-x}Ti_xFeO_3$ nanocrystals – both in the bulk and at the surface, as revealed by XRD and XPS – explains the strong increase in the robustness of the substituted catalysts that leads essentially to the suppression of iron leaching. We cannot rule out that the α-Fe_2O_3 minority phase is subjected to negligible Fe leaching,[62,63] nevertheless remaining below the detection threshold, so that its role in the catalytic performance can be discarded.

Finally, degradation of myclobutanil was studied in order to broaden the scope of the study and confirm further the interest of this new dual SG-LFO catalyst. Similarly, Table 5 clearly shows the superiority of the SG-LFO catalyst in terms of both myclobutanil and TOC removal rates, as well as catalyst robustness.

Stability tests of the SG-LFO catalyst

Considering the robustness of the SG-LFO catalyst in the first test cycle, its stability was further studied in terms of activity, iron release and structural features during recycling tests. Actually, the refinement of the XRD patterns of the used catalysts reveals the structural stability of the $La_{1-x}Ti_xFeO_3$ catalysts during recycling tests (Table 1 and Fig. S4 and Table S2†). Thus, no extra-phase formation occurred under UV-A during the reaction, and no change in terms of the Ti → La substitution rate within the $LaFeO_3$ network and the mean crystallite size has been observed. Regarding the activity, the results of the recycling tests shown in Fig. 9 and Table 3 demonstrate the very good stability and consequently the

Table 4 Kinetic rate constants of 4-CP oxidation and mineralization through pure photocatalysis. Operating conditions: $[4\text{-CP}]_0$ = 25 mg L^{-1}; T = 25 °C; [cat] = 0.5 g L^{-1}; UV-A irradiance of 60 W m^{-2}

Catalyst	k (4-CP),[a] min^{-1}	r_0 (TOC),[b] mg L^{-1} min^{-1}
LFO	0.4 10^{-3}	0.2 10^{-3}
P25-LFO	1.8 10^{-3}	0.3 10^{-3}
SG-LFO	2.8 10^{-3}	0.5 10^{-3}

[a] The 4-CP concentration evolution curve was fitted by a pseudo first-order kinetic model as usually applied. [b] The TOC concentration evolution curve was fitted with a zero-order kinetic model as usually applied.

Table 5 Kinetic rate constants of myclobutanil oxidation and mineralization through the combined catalytic photo-Fenton and photocatalytic AOP over the pristine and the Ti-substituted $LaFeO_3$ catalysts. The concentration of the leached Fe is also reported. Conditions: $[\text{myclobutanil}]_0$ = 20 mg L^{-1}; $[H_2O_2]_0$ = 125 mg L^{-1}; T = 25 °C; [cat] = 0.5 g L^{-1}; UV-A irradiance of 60 W m^{-2}

Catalyst	k (myclobutanil),[a] min^{-1}	r_0 (TOC),[a] mg L^{-1} min^{-1}	[Fe] leached, mg L^{-1}
LFO	0.18	2.3 10^{-2}	2.4
P25-LFO	0.25	2.4 10^{-2}	0.10
SG-LFO	0.38	5.8 10^{-2}	<0.001[b]

[a] The myclobutanil and the TOC concentration evolution curves were fitted by a pseudo first-order model and a zero-order kinetic model as usually applied. [b] The detection limit of Fe leached in the solution was measured at 0.001 ppm.

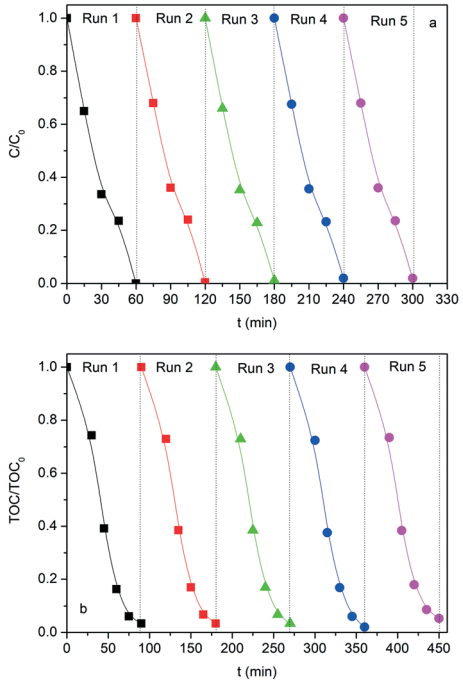

Fig. 9 Catalyst recycling efficiency expressed in terms of time-evolution of both (a) the C/C_0 and (b) the TOC/TOC_0 relative concentrations for 5 consecutive runs in the combined photo-Fenton and photocatalytic degradation of 4-CP with the reused SG-LFO catalyst. Conditions: $[4\text{-CP}]_0$ = 25 mg L^{-1}; $[H_2O_2]_0$ = 125 mg L^{-1}; T = 25 °C; [cat] = 0.5 g L^{-1}; UV-A irradiance of 60 W m^{-2}. The catalyst recovery was achieved by powder filtration.

reusability of the SG-LFO catalyst. Indeed, the apparent kinetic constants for 4-CP and TOC removal remained essentially unchanged after five consecutive runs, and the Fe release in the solution was below the detection threshold (*i.e.* lower than 0.0009% relative to the catalyst Fe content).

Conclusions

To sum up, we have highlighted the interest of using a new and highly robust Ti-substituted $LaFeO_3$ dual catalyst, active in water treatment as a reusable heterogenized photo-Fenton catalyst and a photocatalyst. The $La_{1-x}Ti_xFeO_3$ dual catalyst with a 11% substitution degree was prepared by modifying a facile Pechini sol–gel route using a dried amorphous titania as a titanium source. The strategy combining both AOPs with a single dual catalyst allowed the $La_{1-x}Ti_xFeO_3$ catalyst to simultaneously take advantage the higher reaction rate of photo-assisted CWPO and the higher mineralization yield of photocatalysis. The partial Ti → La cation substitution in the $LaFeO_3$ perovskite network led to pure heterogeneous surface reactions with an increase in the catalyst robustness by more than two orders of magnitude, evidenced by the complete inhibition of the Fe release in water and the stability of the catalytic performance over five test cycles. It further strongly increased the reaction rates, due to both the enhanced availability of the photogenerated charge carriers at the surface and the electronic enrichment of the surface iron, and allowed full mineralization of a pollutant to be achieved at circumneutral pH through combined AOPs.

Forthcoming studies will be concerned with the use of solar light for taking advantage of the narrow band gap of the dual $La_{1-x}Ti_xFeO_3$ catalysts, as well as with downsizing the $La_{1-x}Ti_xFeO_3$ crystallites for increasing further the availability of Fe ions at the catalyst surface.

Conflicts of interest

There are no conflicts to declare.

Acknowledgements

The authors want to thank the European Fund for Regional Development (EFRE/FEDER) for funding the project PHOTOPUR which is performed within the framework of the Interreg V program and Offensive Sciences call. F. Fresno thanks financial support from project SOLPAC: ENE2017-89170-R from the Ministry of Science, Innovation and Universities. T. Dintzer (ICPEES) and D. Ihiawakrim (IPCMS) are thanked for performing the SEM and TEM characterization, respectively. V. Papaefthimiou and S. Zafeiratos (ICPEES) are thanked for performing the XPS and UPS measurements.

Notes and references

1 Y. Chen, G. Zhang, H. Liu and J. Qu, Confining Free Radicals in Close Vicinity to Contaminants Enables Ultrafast Fenton-like Processes in the Interspacing of MoS_2 Membranes, *Angew. Chem., Int. Ed.*, 2019, **58**, 8134–8138.
2 A. M. Braun, Photochemical Purification of Water and Air, *Angew. Chem., Int. Ed.*, 2003, **42**, 5117–5117.
3 L. Ma, Y. Liu, Y. Liu, S. Jiang, P. Li, Y. Hao, P. Shao, A. Yin, X. Feng and B. Wang, Ferrocene-Linkage-Facilitated Charge Separation in Conjugated Microporous Polymers, *Angew. Chem., Int. Ed.*, 2019, **58**, 4221–4226.
4 S. Navalon, R. Martin, M. Alvaro and H. Garcia, Gold on Diamond Nanoparticles as a Highly Efficient Fenton Catalyst, *Angew. Chem., Int. Ed.*, 2010, **49**, 8403–8407.
5 M. Sun, C. Chu, F. Geng, X. Lu, J. Qu, J. Crittenden, M. Elimelech and J. Kim, Reinventing Fenton Chemistry: Iron Oxychloride Nanosheet for pH-Insensitive H_2O_2 Activation, *Environ. Sci. Technol. Lett.*, 2018, **5**, 186–191.
6 P. Bautista, A. F. Mohedano, J. A. Casas, J. A. Zazo and J. J. Rodriguez, An overview of the application of Fenton oxidation to industrial wastewaters treatment, *J. Chem. Technol. Biotechnol.*, 2008, **83**, 1323–1338.
7 R. Chen and J. J. Pignatello, Role of Quinone Intermediates as Electron Shuttles in Fenton and Photoassisted Fenton Oxidations of Aromatic Compounds, *Environ. Sci. Technol.*, 1997, **31**, 2399–2406.
8 J. A. Zazo, J. A. Casas, A. F. Mohedano, M. A. Gilarranz and J. J. Rodríguez, Chemical pathway and kinetics of phenol oxidation by Fenton's reagent, *Environ. Sci. Technol.*, 2005, **39**, 9295–9302.

9 S. Malato, P. Fernández-Ibáñez, M. I. Maldonado, J. Blanco and W. Gernjak, Decontamination and disinfection of water by solar photocatalysis: Recent overview and trends, *Catal. Today*, 2009, **147**, 1–59.
10 A. Verma, D. Dixit, A. Toor and J. Srivastava, Heterogeneous photocatalytic degradation of 2-chloro-4-nitrophenol using slurry and fixed bed reactor, *Environ. Prog. Sustainable Energy*, 2015, **34**, 380–386.
11 A. Goi and M. Trapido, Hydrogen peroxide photolysis, Fenton reagent and photo-Fenton for the degradation of nitrophenols: a comparative study, *Chemosphere*, 2002, **46**, 913.
12 J. A. Zazo, J. A. Casas, A. F. Mohedano and J. J. Rodríguez, Catalytic wet peroxide oxidation of phenol with a Fe/active carbon catalyst, *Appl. Catal., B*, 2006, **65**, 261–268.
13 M. Hartmann, S. Kullmann and H. Keller, Wastewater treatment with heterogeneous Fenton-type catalysts based on porous materials, *J. Mater. Chem.*, 2010, **20**, 9002–9017.
14 M. E. Zarazua-Morin, L. M. Torres-Martinez, E. Moctezuma, I. Juarez-Ramirez and B. B. Zermeno, Synthesis, characterization, and catalytic activity of $FeTiO_3/TiO_2$ for photodegradation of organic pollutants with visible light, *Res. Chem. Intermed.*, 2016, **42**, 1029–1043.
15 A. Sivakumar, A. Selvaraj, A. Ramasamy and V. Balasubramanian, Enhanced Photocatalytic Degradation of Reactive Dyes over $FeTiO_3/TiO_2$ Heterojunction in the Presence of H_2O_2, *Water, Air, Soil Pollut.*, 2013, **224**, 5.
16 R. Dhinesh Kumar, R. Thangappan and R. Jayavel, Synthesis and characterization of $LaFeO_3/TiO_2$ nanocomposites for visible light photocatalytic activity, *J. Phys. Chem. Solids*, 2017, **101**, 25–33.
17 S. Yu, Y. Wang, F. Sun, R. Wang and Y. Zhou, Novel mpg-C_3N_4/TiO_2 nanocomposite photocatalytic membrane reactor for sulfamethoxazole photodegradation, *Chem. Eng. J.*, 2018, **337**, 183–192.
18 C. Cai, Z. Zhang, J. Liu, N. Shan, H. Zhang and D. D. Dionysiou, Visible light-assisted heterogeneous Fenton with $ZnFe_2O_4$ for the degradation of Orange II in water, *Appl. Catal., B*, 2016, **182**, 456–468.
19 H. Mechakra, T. Sehili, M. A. Kribeche, A. A. Ayachi, S. Rossignol and C. George, Use of natural iron oxide as heterogeneous catalyst in photo-Fenton-like oxidation of chlorophenylurea herbicide in aqueous solution: Reaction monitoring and degradation pathways, *J. Photochem. Photobiol., A*, 2016, **317**, 140–150.
20 T. Soltani and B. Lee, Improving heterogeneous photo-Fenton catalytic degradation of toluene under visible light irradiation through Ba-doping in $BiFeO_3$ nanoparticles, *J. Mol. Catal. A: Chem.*, 2016, **425**, 199–207.
21 W. Wang, M. Xu, X. Xu, W. Zhou and Z. Shao, Perovskite Oxide-Based Electrodes for High-Performance Photoelectrochemical Water Splitting: A Review, *Angew. Chem., Int. Ed.*, 2020, **59**(1), 136–152.
22 M. Monai, M. Melchionna and P. Fornasiero, *Chapter One - From metal to metal-free catalysts: Routes to sustainable chemistry*, Academic Press, 2018.
23 E. J. Rosenfeldt and K. G. Linden, Degradation of Endocrine Disrupting Chemicals Bisphenol A, Ethinyl Estradiol, and Estradiol during UV Photolysis and Advanced Oxidation Processes, *Environ. Sci. Technol.*, 2004, **38**, 5476–5483.
24 J. Matos, J. Laine and J.-M. Herrmann, Effect of the Type of Activated Carbons on the Photocatalytic Degradation of Aqueous Organic Pollutants by UV-Irradiated Titania, *J. Catal.*, 2001, **200**(1), 10–20.
25 E. Tütem, R. Apak and Ç F. Ünal, Adsorptive removal of chlorophenols from water by bituminous shale, *Water Res.*, 1998, **32**, 2315–2324.
26 D. A. Haith, Ecological risk assessment of pesticide runoff from grass surfaces, *Environ. Sci. Technol.*, 2010, **44**, 6496–6502.
27 P. Garcia-Muñoz, W. Dachtler, B. Altmayer, R. Schulz, D. Robert, F. Seitz, R. Rosenfeldt and N. Keller, Reaction pathways, kinetics and toxicity assessment during the photocatalytic degradation of glyphosate and myclobutanil pesticides: Influence of the aqueous matrix, *Chem. Eng. J.*, 2020, **384**, 1233152020.
28 P. V. Gosavi and R. B. Biniwale, Pure phase $LaFeO_3$ perovskite with improved surface area synthesized using different routes and its characterization, *Mater. Chem. Phys.*, 2010, **119**, 324–329.
29 X. Qi, J. Zhou, Z. Yue, Z. Gui and L. Li, A simple way to prepare nanosized $LaFeO_3$ powders at room temperature, *Ceram. Int.*, 2003, **29**, 347–349.
30 L. B. McCusker, R. B. Von Dreele, D. E. Cox, D. Louër and P. Scardi, Rietveld refinement guidelines, *J. Appl. Crystallogr.*, 1999, **32**, 36–50.
31 J. Rodríguez-Carvajal, Recent advances in magnetic structure determination by neutron powder diffraction, *Phys. B*, 1993, **192**(1), 55–69.
32 J. Luo, R. Li, Y. Chen, X. Zhou, X. Ning, L. Zhan, L. Ma, X. Xu, L. Xu and L. Zhang, Rational design of Z-scheme $LaFeO_3/SnS_2$ hybrid with boosted visible light photocatalytic activity towards tetracycline degradation, *Sep. Purif. Technol.*, 2019, **210**, 417–430.
33 M. S. S. Doniach, Many-electron singularity in X-ray photoemission and X-ray line spectra from metals, *J. Phys. C: Solid State Phys.*, 1970, **3**, 285.
34 D. A. Shirley, High-Resolution X-Ray Photoemission Spectrum of the Valence Bands of Gold, *Phys. Rev. B: Solid State*, 1972, **5**, 4709–4714.
35 M. Pera-Titus, V. García-Molina, M. A. Baños, J. Giménez and S. Esplugas, Degradation of chlorophenols by means of advanced oxidation processes: a general review, *Appl. Catal., B*, 2004, **47**, 219–256.
36 G. Eisenberg, Colorimetric Determination of Hydrogen Peroxide, *Ind. Eng. Chem., Anal. Ed.*, 1943, **15**(5), 327–328.
37 E. B. Sandell, Colorimetric Determination of Traces of Metals, *J. Phys. Chem.*, 1945, **49**(3), 263–264.
38 R. D. Shannon, Revised effective ionic radii and systematic studies of interatomic distances in halides and chalcogenides, *Acta Crystallogr., Sect. A: Cryst. Phys., Diffr., Theor. Gen. Crystallogr.*, 1976, **32**, 751–767.

39 T. S. Jamil, H. A. Abbas, R. A. Nasr and R. Vannier, Visible light activity of $BaFe_{1-x}Cu_xO_{3-\delta}$ as photocatalyst for atrazine degradation, *Ecotoxicol. Environ. Saf.*, 2018, **163**, 620–628.

40 S. K. Rashmi, H. S. Bhojya Naik, H. Jayadevappa, R. Viswanath, S. B. Patil and M. Madhukara Naik, Solar light responsive Sm-Zn ferrite nanoparticle as efficient photocatalyst, *Mater. Sci. Eng., B*, 2017, **225**, 86–97.

41 M. R. De Guire, R. C. O'Handley and G. Kalonji, The cooling rate dependence of cation distributions in $CoFe_2O_4$, *J. Appl. Phys.*, 1989, **65**, 3167–3172.

42 Z. J. Zhang, Z. L. Wang, B. C. Chakoumakos and J. S. Yin, Temperature Dependence of Cation Distribution and Oxidation State in Magnetic Mnâ'Fe Ferrite Nanocrystals, *J. Am. Chem. Soc.*, 1998, **120**, 1800–1804.

43 T. T. N. Phan, A. N. Nikoloski, P. A. Bahri and D. Li, Heterogeneous photo-Fenton degradation of organics using highly efficient Cu-doped $LaFeO_3$ under visible light, *J. Ind. Eng. Chem.*, 2018, **61**, 53–64.

44 L. Hou, G. Sun, K. Liu, Y. Li and F. Gao, Preparation, characterization and investigation of catalytic activity of Li-doped $LaFeO_3$ nanoparticles, *J. Sol-Gel Sci. Technol.*, 2006, **40**, 9–14.

45 Y. Ye, H. Yang and R. Li, Enhanced photocatalytic performance and mechanism of Ag-decorated $LaFeO_3$ nanoparticles, *J. Sol-Gel Sci. Technol.*, 2017, **82**, 509–518.

46 J. Liqiang, Q. Yichun, W. Baiqi, L. Shudan, J. Baojiang, Y. Libin, F. Wei, F. Honggang and S. Jiazhong, Review of photoluminescence performance of nano-sized semiconductor materials and its relationships with photocatalytic activity, *Sol. Energy Mater. Sol. Cells*, 2006, **90**(12), 1773–1787.

47 S. Bharathkumar, M. Sakar and S. Balakumar, Experimental Evidence for the Carrier Transportation Enhanced Visible Light Driven Photocatalytic Process in Bismuth Ferrite ($BiFeO_3$) One-Dimensional Fiber Nanostructures, *J. Phys. Chem. C*, 2016, **120**, 18811–18821.

48 L. Collado, A. Reynal, F. Fresno, M. Barawi, C. Escudero, V. Perez-Dieste, J. M. Coronado, D. P. Serrano, J. R. Durrant and L. P. de, Unravelling the effect of charge dynamics at the plasmonic metal/semiconductor interface for CO_2 photoreduction, *Nat. Commun.*, 2018, **9**, 4986.

49 A. Charanpahari, S. S. Umare and R. Sasikala, Effect of Ce, N and S multi-doping on the photocatalytic activity of TiO_2, *Appl. Surf. Sci.*, 2013, **282**, 408–414.

50 S. Y. Smolin, A. K. Choquette, J. Wang, S. J. May and J. B. Baxter, Distinguishing Thermal and Electronic Effects in Ultrafast Optical Spectroscopy Using Oxide Heterostructures, *J. Phys. Chem. C*, 2018, **122**, 115–123.

51 R. Sasikala, A. R. Shirole, V. Sudarsan, K. G. Girija, R. Rao, C. Sudakar and S. R. Bharadwaj, Improved photocatalytic activity of indium doped cadmium sulfide dispersed on zirconia, *J. Mater. Chem.*, 2011, **21**, 16566–16573.

52 S. Phokha, S. Pinitsoontorn, S. Rujirawat and S. Maensiri, Polymerized complex synthesis and effect of Ti dopant on magnetic properties of $LaFeO_3$ nanoparticles, *J. Nanosci. Nanotechnol.*, 2015, **15**, 9171–9177.

53 S. Thirumalairajan, K. Girija, V. Ganesh, D. Mangalaraj, C. Viswanathan and N. Ponpandian, Novel Synthesis of $LaFeO_3$ Nanostructure Dendrites: A Systematic Investigation of Growth Mechanism, Properties, and Biosensing for Highly Selective Determination of Neurotransmitter Compounds, *Cryst. Growth Des.*, 2013, **13**, 291–302.

54 M. Humayun, N. Sun, F. Raziq, X. Zhang, R. Yan, Z. Li, Y. Qu and L. Jing, Synthesis of ZnO/Bi-doped porous $LaFeO_3$ nanocomposites as highly efficient nano-photocatalysts dependent on the enhanced utilization of visible-light-excited electrons, *Appl. Catal., B*, 2018, **231**, 23–33.

55 S. Petrović, A. Terlecki-Baričević, L. Karanović, P. Kirilov-Stefanov, M. Zdujić, V. Dondur, D. Paneva, I. Mitov and V. Rakić, $LaMO_3$ (M=Mg, Ti, Fe) perovskite type oxides: Preparation, characterization and catalytic properties in methane deep oxidation, *Appl. Catal., B*, 2008, **79**(2), 186–198.

56 T. Yamashita and P. Hayes, Analysis of XPS spectra of Fe^{2+} and Fe^{3+} ions in oxide materials, *Appl. Surf. Sci.*, 2008, **254**, 2441–2449.

57 D. D. Hawn and B. M. DeKoven, Deconvolution as a correction for photoelectron inelastic energy losses in the core level XPS spectra of iron oxides, *Surf. Interface Anal.*, 1987, **10**, 63–74.

58 J. C. Yu, J. Yu, W. Ho, Z. Jiang and L. Zhang, Effects of F-Doping on the Photocatalytic Activity and Microstructures of Nanocrystalline TiO_2 Powders, *Chem. Mater.*, 2002, **14**, 3808–3816.

59 D. L. Sedlak and A. W. Andren, Oxidation of Chiorobenzene with Fenton's Reagent, *Environ. Sci. Technol.*, 1991, **25**, 777–782.

60 M. E. Balmer and B. Sulzberger, Atrazine degradation in irradiated iron/oxalate systems: Effects of pH and oxalate, *Environ. Sci. Technol.*, 1999, **33**, 2418–2424.

61 G. Pliego, J. A. Zazo, P. Garcia-Muñoz, M. Munoz, J. A. Casas and J. J. Rodriguez, Trends in the Intensification of the Fenton Process for Wastewater Treatment: An Overview, *Crit. Rev. Environ. Sci. Technol.*, 2015, **45**, 2611–2692.

62 R. Prucek, M. Hermanek and R. Zbořil, An effect of iron(III) oxides crystallinity on their catalytic efficiency and applicability in phenol degradation—A competition between homogeneous and heterogeneous catalysis, *Appl. Catal., A*, 2009, **366**(2), 325–332.

63 G. Carraro, C. Maccato, A. Gasparotto, T. Montini, S. Turner, O. I. Lebedev, V. Gombac, G. Adami, G. Van Tendeloo, D. Barreca and P. Fornasiero, Enhanced Hydrogen Production by Photoreforming of Renewable Oxygenates Through Nanostructured Fe_2O_3 Polymorphs, *Adv. Funct. Mater.*, 2014, **24**, 372–378.

